Kekulé Induced Valley Birefringence and Skew Scattering in Graphene

Elias Andrade,[1, *] Ramon Carrillo-Bastos,[2] Mahmoud M. Asmar,[3] and Gerardo G. Naumis[4]

[1]*Posgrado en Ciencias Físicas, Instituto de Física,*
Universidad Nacional Autónoma de México (UNAM). Apdo. Postal 20-364, 01000 México D.F., México
[2]*Facultad de Ciencias, Universidad Autónoma de Baja California,*
Apdo. Postal 1880, 22800 Ensenada, Baja California, México.
[3]*Department of Physics, Kennesaw State University, Marietta, Georgia 30060, U.S.A.*
[4]*Depto. de Sistemas Complejos, Instituto de Física,*
Universidad Nacional Autónoma de México (UNAM). Apdo. Postal 20-364, 01000 México D.F., México
(Dated: August 8, 2022)

In graphene, a Kekulé-Y bond texture modifies the electronic band structure generating two concentric Dirac cones with different Fermi velocities lying in the Γ-point in reciprocal space. The energy dispersion results in different group velocities for each isospin component at a given energy. This energy spectrum combined with the negative refraction index in p-n junctions, allows the emergence of an electronic analog of optical birefringence in graphene. We characterize the valley birefringence produced by a circularly symmetric Kekulé patterned and gated region using the scattering approach. We found caustics with two cusps separated in space by a distance dependent on the Kekulé interaction and that provides a measure of its strength. Then, at low carrier concentration we find a non-vanishing skew cross section, showing the asymmetry in the scattering of electrons around the axis of the incoming flux. This effect is associated with the appearance of the valley Hall effect as electrons with opposite valley polarization are deflected towards opposite directions.

I. INTRODUCTION

The similarities between the Helmholtz and Schrödinger equations result in photons and electrons displaying similar wave phenomena[1]. Furthermore, the propagation of electrons through the two-dimensional honeycomb arrangement of carbon atoms, known as graphene, leads to the dressing of electronic states as massless Dirac-like electronic excitations residing at opposite corners of the Brillouin zone[2], thus augmenting the analogies between the electronic and optical phenomena. The ability to control the charge carrier's group velocity via graphene gating[3] has led to the prediction and experimental realization of electronic Veselago lensing[4,5]. The sensitivity of this lensing to the conduction electrons properties aids the detection of anisotropies and tilting of the Dirac cones[6,7], the presence of strain[8], and disorder[9]. Veselago lensing also facilitates the waveguiding of electrons in p-n junctions[10] and the emergence of caustics and cusps in circular geometries[11]. Moreover, similar to optical birefringence in anisotropic crystals where the group velocity depends on light polarization[12], spin birefringence for electrons emerges in graphene due to the Rashba spin-orbit interaction[13,14] which leads to distinct Fermi velocities for each spin component, and in circular geometries, spin birefringence brings about the formation of caustics with two cusps, with a space separation that depends on the strength of the Rashba spin-orbit coupling[15,16].

In addition to spin, electrons in graphene possess the valley degree of freedom[17]. The valleys in graphene have a large separation in momentum space[18], which suggests that this degree of freedom can be potentially used in applications where it will play a role similar to spin in spintronics[19,20]. The field that aims to manipulate and con-

trol the valley degree of freedom in applications is known as *valleytronics*[21–33]. Similar to spin-orbit interactions in spintronics, interactions contrasting the degenerate valleys in graphene play an essential role in valleytronincs. Such interactions include the Kekulé patterning of graphene[34,35],*i.e.*, the periodic bond modulation of the graphene lattice. Depending on the bond modulation pattern[36] two different Kekulé distortions phases can emerge: the Kekulé-Y[37] found in graphene deposited on Cu[111] and the Kekulé-O[38–42] that arises in bilayer graphene intercalated with Li. The tight-binding calculations by Gamayun *et al.*[36] found that Kekulé-Y produces an effective interaction that leads to valley-momentum locking, while Kekulé-O leads to the formation of a gap in the electronic spectrum.

Kekulé-Y patterned graphene, breaks a valley degeneracy through valley-momentum locking which produces a low energy spectrum with two nested Dirac cones with different Fermi velocities[36]. The energy-momentum dispersion modification caused by Kekulé-Y patterning leads to drastic modifications in the magnetic and optical response of graphene[43–48], and crucially aids the control of the valley degree of freedom in the electronic transport[49–56]. In this paper we study the scattering of Dirac fermions from circularly Kekulé-Y-patterned regions in the semiclassical limit and we explore the effects of this interaction on electron optics and the appearance of valley birefringence. We also investigate the scattering of charge carriers in graphene from short-range scattering regions with locally enhance Kekulé-Y interactions due to adatom deposition. Our analysis of the total, transport, and skew cross sections for these short-range scatterers reveals the dependence of these cross sections on the strength of the Kekulé-Y interaction and we show the appearance of a valley Hall effects due to skew scattering

from these scatterers.

The layout of this work is as follows. In section II we present the model, section III is devoted the scattering calculations. Valley birefringence is analyzed in section IV, while in section V we study the low-energy scattering. Finally, we conclude by discussing our main findings.

II. MODEL

Our system consist of an infinite sheet of pristine graphene containing a circularly Kekulé-ordered patch of radius R, Fig. 1. We consider the scattering of an incoming flux of electrons in the x-direction with momentum k. To describe the electronic properties of the graphene sheet we adopt the low-energy description, i.e., the Dirac Hamiltonian[18]. Nevertheless, the Kekulé modulated portion of the lattice has a larger unit cell than non-modulated graphene lattice. Hence, to match the pristine and Kekulé patterned graphene wave functions it is practical to use an enlarged unitary cell for the case of undistorted graphene. This is equivalent to consider the group C_{6v}'', with a cell with six atom graphene's unit cell, which avoids the treatment of degenerate states at two inequivalent Dirac points[57]. This is more clearly seen if we start with the Hamiltonian for the Kekulé region and then pristine graphene appears as a limiting case.
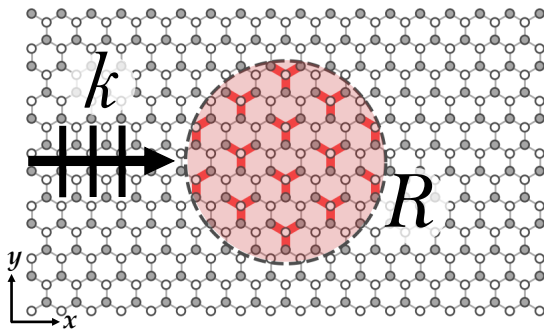

FIG. 1. Schematic of the system (not to scale). A graphene lattice where an incoming flux of electrons in the x direction approaches a circular region of radius R with a gate potential and Kekulé-Y bond texture (red bonds).

The space dependent Hamiltonian describing the system in Fig. 1 is given by

$$\mathcal{H} = \mathcal{H}_0 + \mathcal{H}_Y(r) + V(r) , \qquad (1a)$$

where,

$$\mathcal{H}_0 = v_f(\boldsymbol{p} \cdot \boldsymbol{\sigma}) \otimes \tau_0 \qquad (1b)$$

is the low-energy graphene Hamiltonian with $\boldsymbol{p} = -i\hbar(\partial_x, \partial_y)$ the momentum operator, $v_f \sim 10^6$m/s the Fermi velocity, and σ, τ the sets of Pauli matrices acting

on the sublattice and valley pseudo-spin spaces respectively.

$$\mathcal{H}_Y = \Delta v_f \sigma_0 \otimes (\boldsymbol{p} \cdot \boldsymbol{\tau})\Theta(R - r) \qquad (1c)$$

is the Kekulé-Y bond perturbation[36] with amplitude Δ within the circular region,

$$V(r) = V_0\Theta(R - r)\sigma_0 \otimes \tau_0, \qquad (1d)$$

is a constant gate potential with amplitude V_0 in the Kekulé circular patch, and Θ is the Heaviside function.

The Hamiltonian in Eq. (1a) acts on the states expressed in the valley isotropic representation:

$$\Psi = \begin{bmatrix} \psi_{K'} \\ \psi_K \end{bmatrix} = \begin{bmatrix} -\psi_{B,K'} \\ \psi_{A,K'} \\ \psi_{A,K} \\ \psi_{B,K} \end{bmatrix}, \qquad (1e)$$

Notice that the subindex A and B in Ψ corresponds to each graphene's bipartite lattice while $\boldsymbol{K}$ and $\boldsymbol{K}'$ label the valley. For regions outside the Kekulé modulated region, the limit of pristine graphene is recovered, $\Delta = 0$, thus having a 4×4 operator which represents the Dirac Hamiltonian in the enlarged unitary cell.

III. SCATTERING

In this section we study the scattering of Dirac fermions from a circularly symmetric Kekulé patterned region. We adopt the partial waves scattering method to find the S-matrix, which requires finding and matching the eigenstates in the different scatttering regions of our system. For any effective theory that uses an envelope wavefunction, as is the case of the Dirac equation for graphene, the matching requires a supplemental boundary condition of the form $\Psi = M\Psi$ in order to retain the hermiticity and preserve currents. Here M is a matrix containing the microscopic details and the symmetries of the problem[58–63]. Since we consider the Kek-Y bond modulation as a perturbation within the same graphene sheet, no major misalignment is expected and thus for small Δ we can consider M as unitary throughout this work. Moreover, as our system possesses circular symmetry, it is natural to evaluate its eigenfunctions in polar coordinates. The z-component of orbital angular momentum $L_z = -i\hbar\partial_\theta$ does not commute with the Hamiltonian, $[H, L_z] = i\hbar v_f(\boldsymbol{\sigma} \times \boldsymbol{p})_z \otimes \tau_0 + i\hbar v_f\sigma_0 \otimes (\boldsymbol{\tau} \times \boldsymbol{p})_z$. On the other hand, the sum of L_z and the intrinsic angular momenta associated with the valley and sublattice degrees of freedom, "valley-lattice-angular momentum" J_z, is conserved and given by

$$J_z = L_z + \frac{\hbar}{2}(\sigma_z \otimes \tau_0 + \sigma_0 \otimes \tau_z). \qquad (2)$$

Here, it is important to notice that $[H, \frac{\hbar}{2}\sigma_z \otimes \tau_0] = -i\hbar v_f(\boldsymbol{\sigma} \times \boldsymbol{p})_z \otimes \tau_0$, and $[H, \frac{\hbar}{2}\sigma_0 \otimes \tau_z] = -i\hbar v_f\sigma_0 \otimes (\boldsymbol{\tau} \times$

$p)_z$, which leads to $[H, \frac{\hbar}{2}\sigma_z \otimes \tau_0 + \frac{\hbar}{2}\sigma_0 \otimes \tau_z + L_z] = 0$. We can express the eigenfunctions in their total pseudo-angular momentum basis, such that $J_z \Psi_n = n\hbar\Psi_n$, thus

$$\Psi_n(r,\theta) = e^{in\theta} \begin{bmatrix} -e^{-i\theta}\Phi_{B,K'}(r) \\ \Phi_{A,K'}(r) \\ \Phi_{A,K}(r) \\ e^{i\theta}\Phi_{B,K}(r) \end{bmatrix}. \tag{3}$$

where $\theta = \tan^{-1} y/x$, and find the radial part of the wave functions by applying the Hamiltonian in Eq. (1a) to our spinor in Eq. (3) to get the following set of coupled differential equations,

$$L_n^-[\Phi_{A,K'}(r) + \Delta\Phi_{A,K}(r)] = -i(\epsilon - \nu)\Phi_{B,K'}(r), \tag{4a}$$

$$L_{n-1}^+\Phi_{B,K'}(r) - \Delta L_{n+1}^-\Phi_{B,K}(r) = -i(\epsilon - \nu)\Phi_{A,K'}(r), \tag{4b}$$

$$L_{n+1}^-\Phi_{B,K}(r) - \Delta L_{n-1}^+\Phi_{B,K'}(r) = i(\epsilon - \nu)\Phi_{A,K}(r), \tag{4c}$$

$$L_n^+[\Phi_{A,K}(r) + \Delta\Phi_{A,K'}(r)] = i(\epsilon - \nu)\Phi_{B,K}(r), \tag{4d}$$

where,

$$L_n^\pm = \left(\partial_r \mp \frac{n}{r}\right), \tag{4e}$$

here $\epsilon = E/(\hbar v_f)$, $\nu = V_0/(\hbar v_f)$. Since $L_n^\pm$ acts as a ladder operator for the cylindrical Bessel functions J_n,

$$L_n^\pm J_n(kr) = \mp k J_{n\pm1}(kr), \tag{5}$$

thus, a natural ansatz is

$$\Phi_{A,K}(r) = i(\epsilon - \nu)C_A J_n(kr), \tag{6}$$
$$\Phi_{A,K'}(r) = i(\epsilon - \nu)C_B J_n(kr), \tag{7}$$

where C_A and C_B are constants, and k is the electron wave number. Inserting the anzats in Eq. (6) in the relations in Eq. (4), results into the exact form of the spinor solutions and determines the wave numbers

$$k_\pm = \frac{|E - V_0|}{\hbar v_f(1 \pm \Delta)}. \tag{8}$$

Thus the nth angular momentum eigenstates in the inner region are,

$$\Psi_n^<(r,\theta) = T_n^+ e^{in\theta} \begin{bmatrix} J_{n-1}(k_+r)e^{-i\theta} \\ is' J_n(k_+r) \\ is' J_n(k_+r) \\ -J_{n+1}(k_+r)e^{i\theta} \end{bmatrix}$$
$$+ T_n^- e^{in\theta} \begin{bmatrix} J_{n-1}(k_-r)e^{-i\theta} \\ is' J_n(k_-r) \\ -is' J_n(k_-r) \\ J_{n+1}(k_-r)e^{i\theta} \end{bmatrix}, \tag{9}$$

where T_n^+ and T_n^- are determined by $s' = \text{sgn}(E - V_0)$ and the boundary conditions. Since the pseudo-angular

momentum is conserved during the scattering process, we can treat each component of n independently and use the partial wave method to determine the S-matrix elements. In the region $r > R$, we describe the wavefunction in terms of incoming (in) and outgoing (out) cylindrical waves, where the corresponding spinor for each valley is

$$\psi_{n,K'}^{(\text{out})/(\text{in})}(r,\theta)\,|K'\rangle = \begin{bmatrix} H_{n-1}^{(1)/(2)}(kr)e^{i(n-1)\theta} \\ is H_n^{(1)/(2)}(kr)e^{in\theta} \end{bmatrix} |K'\rangle, \tag{10a}$$

$$\psi_{n,K}^{(\text{out})/(\text{in})}(r,\theta)\,|K\rangle = \begin{bmatrix} -is H_n^{(1)/(2)}(kr)e^{in\theta} \\ H_{n+1}^{(1)/(2)}(kr)e^{i(n+1)\theta} \end{bmatrix} |K\rangle, \tag{10b}$$

here $H_n^{(1)}$ and $H_n^{(2)}$ are Hankel functions of the first and second kind respectively, and $s = \text{sgn}(E)$. Now we can write the wavefunctions in terms of the scattering matrix S_n such that $\psi_n = \psi_n^{(\text{in})} + S_n\psi_n^{(\text{out})}$,

$$\Psi_n^>(r,\theta) = \sum_\alpha c_\alpha \psi_{n,\alpha}^{(\text{in})}(r,\theta)\,|\alpha\rangle$$
$$+ \sum_{\alpha,\beta} c_\alpha S_{n,\alpha\beta}\psi_{n,\beta}^{(\text{out})}(r,\theta)\,|\beta\rangle, \tag{11}$$

where $\alpha, \beta \in \{K, K'\}$ and $S_{n,\alpha\beta}$ corresponds to the scattering from α to β valley, c_K and $c_{K'}$ are the weights of the valley polarization. We can obtain the coefficients for S_n, T_n^+ and T_n^- by applying the boundary conditions at $\Psi_n^<(R,\theta) = \Psi_n^>(R,\theta)$, as shown in Appendix A. Additionally, an incident plane-wave in the x-direction can be expressed with the aid of the Jacobi-Anger expansion as,

$$e^{ikr\cos\theta} = \sum_{n=-\infty}^{\infty} i^n J_n(kr)e^{in\theta}, \tag{12}$$

or equivalently as,

$$\Phi_0(r,\theta) = \sum_{n=-\infty}^{\infty} \sum_\alpha c_\alpha \frac{i^n}{2}[\psi_{n,\alpha}^{(\text{out})}(r,\theta) + \psi_{n,\alpha}^{(\text{in})}(r,\theta)]\,|\alpha\rangle. \tag{13}$$

The latter allows one to express $\Psi^>(r,\theta)$ in terms of the incoming plane and the outgoing waves, i.e.

$$\Psi^>(r,\theta) = \Phi_0(r,\theta)$$
$$+ \sum_{n=-\infty}^{\infty} \sum_{\substack{\alpha=K,K' \\ \bar\alpha\neq\alpha}} c_\alpha \frac{i^n}{2}\Big[(S_{n,\alpha\alpha} - 1)\psi_{n,\alpha}^{(\text{out})}(r,\theta)\,|\alpha\rangle$$
$$+ S_{n,\alpha\bar\alpha}\psi_{n,\bar\alpha}^{(\text{out})}(r,\theta)\,|\bar\alpha\rangle\Big], \tag{14}$$

and the total wave function is obtained by,

$$\Psi(r,\theta) = \sum_{n=-\infty}^{\infty} \left[\Psi_n^<(r,\theta) + \Psi_n^>(r,\theta)\right]. \tag{15}$$

IV. VALLEY BIREFRINGENCE

Partially subjecting a graphene sheet to a gate potential that reverses its carriers character from electrons to holes between gated and non-gated regions leads to many interesting analogies between its electron dynamics and optical phenomena[4,11,15] The key ingredient to this phenomena is the reversal of the group velocity of quasiparticles between the regions with and without gate potentials. For example, if we consider a circularly gated region on graphene (Fig. 1 with V_0 and taking $\Delta = 0$), then, in the outer region, $r > R$, a quasiparticle's group velocity is $v_g^> = v_f(k_{x,r>R}\hat{x} + k_{y,r>R}\hat{y})/|k_{r>R}|$, while in the inner region we have a negative group velocity $v_g^< = -v_f(k_{x,r<R}\hat{x} + k_{y,r<R}\hat{y})/|k_{r<R}|$, here $k_{r<R}$ ($k_{r>R}$) is the wavevector in the inner (outer) region. The reversal of the group velocity from the outer to the inner region indicates that the gated region will act, in the semiclassical limit, as a circular electronic lens with a negative index of refraction $n = -k_{r<R}/k_{r>R}$, where $k_{r<R}$ is the wave number inside the gated patch and $k_{r>R}$ outside, and n is deduced from the electronic Snell's law[4,17]. As shown in Fig. 1, in the limit $kR \gg 1$, the negative index of refraction leads to constructive interference between the different partial wave components and results in a probability density that forms cardioid caustics and cusps[11], in what mimics the optical caustics which arise from light refraction through a shaped medium and belong to a class of cusps in catastrophe theory[12]. Using differential geometry[11], the positions of the cusps for each $p - 1$ internal reflections can be shown to be

$$x_{cusp}(p) = \frac{(-1)^p}{|n| - 1 + 2p}R, \qquad (16)$$

and in the case shown in Fig. 2 a), as the amplitude decreases with each internal reflection, we can clearly distinguish the cusps corresponding to $p = 1, 2$.

If in addition to the gate potential the circular region contains the Kekulé bond texture, then the electronic bands in this region will be characterized by $E_\pm = \pm\hbar v_f(1 \pm \Delta)|\boldsymbol{k}| + V_0$. Therefore, the gating of this region leads to the Fermi level intersecting the two degenerate hole bands, which are characterized by the two group velocities, $v_{g,\pm} = -v_f(1 \pm \Delta)$. Then, when $\Delta \neq 0$, in addition to the sign reversal of the group velocity between both regions we also have the two different group velocities in the inner region. Hence, the Kekulé patterned and gated region will act as a circular lens with two negative indices of refraction

$$n_\pm = -\frac{k_{\pm,r<R}}{k_{r>R}}, \qquad (17)$$

with $k_{\pm,r<R} = k_+, k_-$ and are given in Eq. (8). As shown in Fig. 2b) The Kekulé patterning of the circular region results into the doubling of the cusps and caustics of the circular lens, which reflects its birefringent nature. The degree of birefringence can be characterized by $\zeta =$

$|n_+ - n_-|$, and for the set of parameters in Fig. 2b) we get $\zeta \approx 0.25$. Moreover, the cusps locations is now modified to

$$x_{cusp}^\pm(p) = \frac{(-1)^p}{|n_\pm| - 1 + 2p}R, \qquad (18)$$

and the spatial separation between the two cusps is found by $|x_{cusp}^+ - x_{cusp}^-|$. In Fig. 2 c) we show the valley preserving amplitude component, $|\psi_{KK}(r)|^2$, and Fig. 2 d) the valley mixing component, $|\psi_{KK'}(r)|^2$. From these figures we can notice that the Kekulé bond texture leads to the oscillation of the valley component as electrons travel in the patterned region, in what mimics the electron's spin-momentum coupling in the presence of a Rashba interaction[13,15].

V. LOW ENERGY SCATTERING

The scattering process can be further analyzed by obtaining the different types of cross sections, such as the total cross section σ_t which tells us the magnitude of the interaction between the incoming flux and the scattering region, the transport cross section σ_{tr} that describes the average momentum transfer during the scattering, and the skew cross section σ_{sk} which shows the asymmetry in the scattering around the axis of the incoming flux. This quantities can be obtained through the scattering amplitude $f(\theta)$, which can be found in the far field limit, $i.e.$, via the asymptotic form of the wave function as $r \to \infty$

$$\Psi(r \to \infty) \to \Phi_0 + \sum_n \sum_{\alpha,\beta} c_\alpha f_{n,\alpha\beta}(\theta)\frac{e^{ikr}}{\sqrt{r}}|\beta\rangle, \qquad (19)$$

and using the asymptotic expansion of the Hankel functions,

$$H_n(kr)^{(1)/(2)} \to \sqrt{\frac{2}{\pi kr}}e^{\pm i(kr - \frac{n\pi}{2} - \frac{\pi}{4})}, \qquad (20)$$

by comparing Eq. (14) to Eq. (19) we can deduce the scattering amplitude for each partial wave component in terms of the S matrix components

$$f_n = \frac{e^{-i\pi/4}}{\sqrt{2\pi k}}\begin{bmatrix} S_{n,K',K'} - 1 & -iS_{n,K',K} \\ iS_{n,K,K'} & S_{n,K,K} - 1 \end{bmatrix}, \qquad (21)$$

where $S_{n,\alpha\beta}$ are the valley preserving ($\alpha = \beta$) and valley mixing scattering ($\alpha \neq \beta$) matrix elements corresponding to the nth partial wave component (α and β represent the Dirac points, either K or K'). Then, for each process (valley preserving and valley mixing), we find the corresponding differential cross section,

$$\sigma_{\alpha\beta}(\theta) = \left|\sum_{n=-\infty}^{\infty} f_{n,\alpha\beta}e^{in\theta}\right|^2, \qquad (22)$$
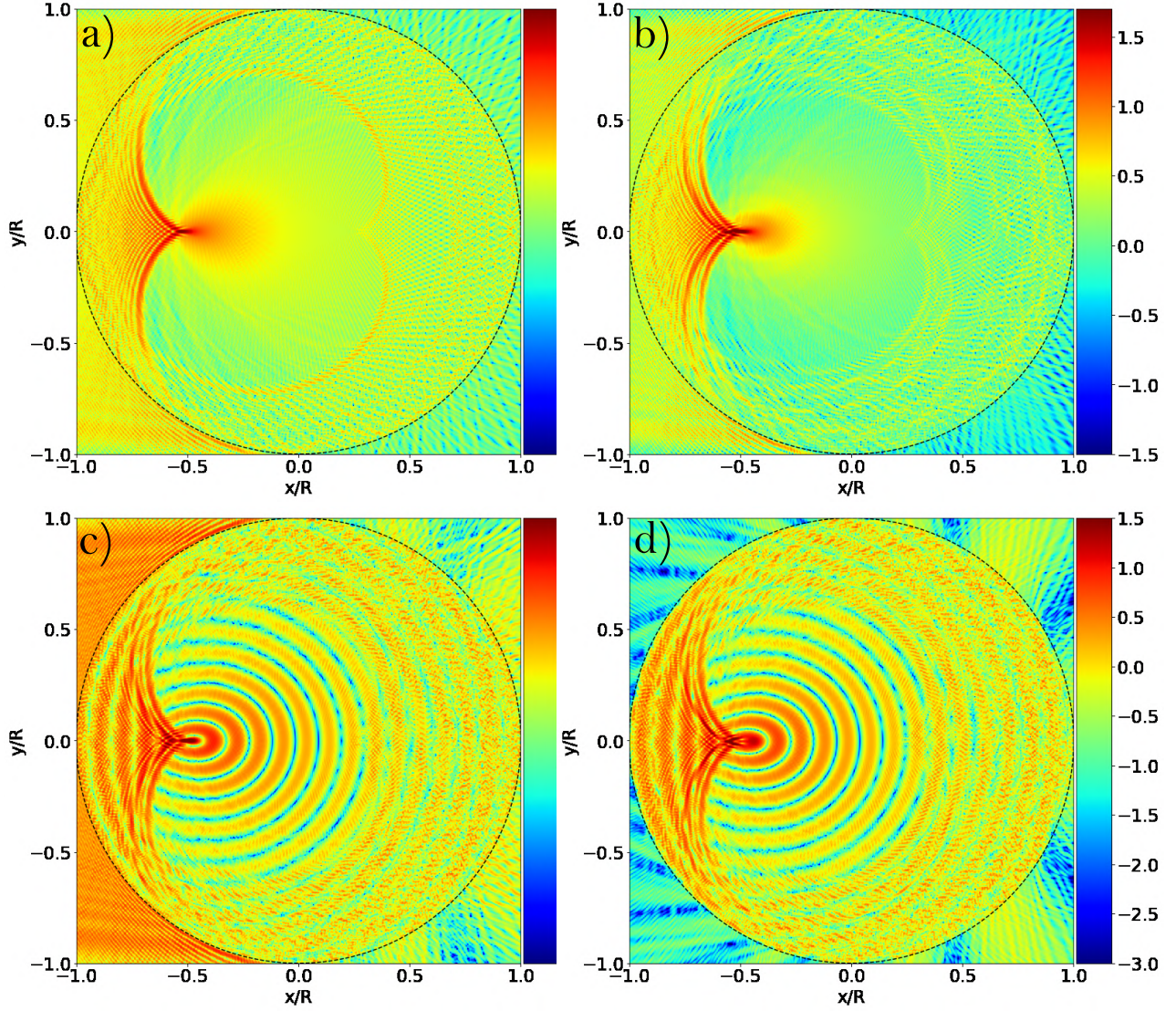
FIG. 2. Space dependence of the probability density (in $\log_{10}$ scale), for an incoming electron flux in the x-direction with valley polarization K' and $kR = 300$. The dashed line shows the boundary between the scattering regions. A gate potential $V_0 R/(\hbar v_f) = 600$ is present in the inner region for, a) pristine graphene, b) Kek-Y distorted graphene in the $r < R$ region with $\Delta = 0.1$. Panel c) shows the valley-preserving component and d) the valley-flip component, for the case described in b).

total cross section,

$$\sigma_{t,\alpha\beta} = \int_{-\pi}^{\pi} \sigma_{\alpha\beta}(\theta)d\theta = 2\pi \sum_{n=-\infty}^{\infty} |f_{n,\alpha\beta}|^2, \qquad (23)$$

transport cross section,

$$\sigma_{tr,\alpha\beta} = \int_{-\pi}^{\pi} \sigma_{\alpha\beta}(\theta)(1 - \cos\theta)d\theta$$

$$= \sigma_{t,\alpha\beta} - 2\pi \sum_{n=-\infty}^{\infty} \mathrm{Re}(f_{n,\alpha\beta}f_{n+1,\alpha\beta}^*), \qquad (24)$$

and the skew cross section,

$$\sigma_{sk,\alpha\beta} = \int_{-\pi}^{\pi} \sigma_{\alpha\beta}(\theta)\sin\theta d\theta$$

$$= 2\pi \sum_{n=-\infty}^{\infty} \mathrm{Im}(f_{n,\alpha\beta}f_{n+1,\alpha\beta}^*), \qquad (25)$$

by summing over all different allowed processes

$$\sigma_\eta = \sum_{\alpha,\beta} \sigma_{\eta,\alpha\beta}, \qquad (26)$$

we obtain the total, transport, and skew cross sections $(\eta \in \{t, tr, sk\})$.

For low carrier concentrations and small regions with Kekulé bond texture ($kR \ll 1$) the most significant scat-

tering channels are those of angular momentum $n = -1, 0, 1$. Within this regime, we show in Fig. 3 the total cross section against the strength of gate potential V_0. In the absence of Kekulé patterning, the total cross sec-
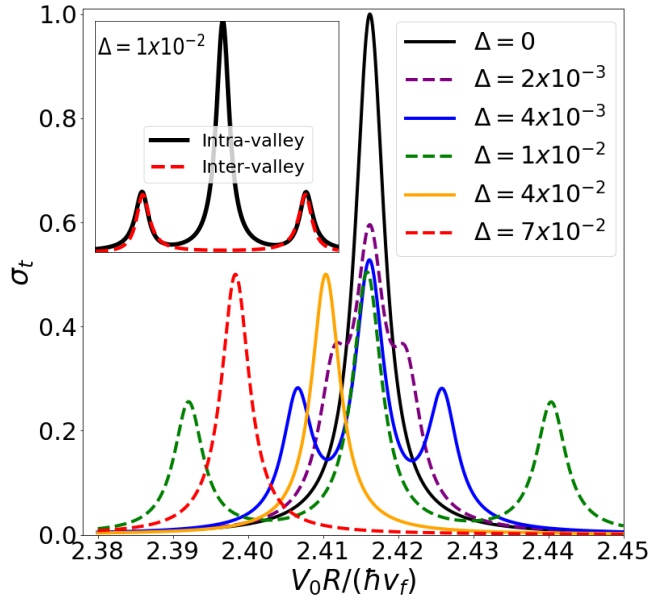

FIG. 3. Total cross section σ_t as a function of V_0 for incoming electrons in the x-direction with $kR = 1.5 \times 10^{-3}$. (Inset) Total cross section for intra-valley $\sigma_{t,KK} + \sigma_{t,K'K'}$ and inter-valley $\sigma_{t,KK'} + \sigma_{t,K'K}$ process with $\Delta = 0.01$.

tion of the gated region displays one peak which uniquely arises from the valley preserving process and indicates the formation of quasi-bound states in this region with finite life-time characterized by the width of the peak[16,64]. An increasing strength of the Kekulé interaction leads to the central (valley-preserving) peak height shrinking and its location shifting, while two new resonant (valley-mixing) peaks emerge. These two new peaks correspond to quasi-bound states forming due to valley mixing processes as it is shown in the inset of Fig. 3, and consequently their height increases with increasing values of Δ, as shown in Fig. 3.

When local interactions in a graphene sheet lead to the breaking of effective time reversal (time reversal per valley) while preserving the total time reversal, as is the case for the Kekulé patterning, it is possible to have a skew scattering, and by symmetry considerations it can be shown that[16]

$$\sigma_{sk,\alpha\alpha} = -\sigma_{sk,\bar{\alpha}\bar{\alpha}}, \tag{27a}$$

$$\sigma_{sk,\alpha\bar{\alpha}} = 0. \tag{27b}$$

The latter equations indicate that electrons with opposite valley polarization get deflected towards opposite directions as they get scattered, thus producing a valley-Hall effect. To measure the asymmetry of the scattering per

valley we calculate the skew parameter γ_V, which is defined as,

$$\gamma_V = \frac{1}{2}(\gamma_K - \gamma_{K'}), \tag{28a}$$

where

$$\gamma_\beta = \frac{\sum_\alpha \sigma_{sk,\alpha\beta}}{\sum_\alpha \sigma_{tr,\alpha\beta}}, \tag{28b}$$

this quantity is directly connected to the transverse valley currents and is equal to the valley Hall angle at zero temperature in the absence of side-jump effects[65],

$$\Theta_{VH} = \frac{j_{VH}}{j_x} = \gamma_V. \tag{29}$$
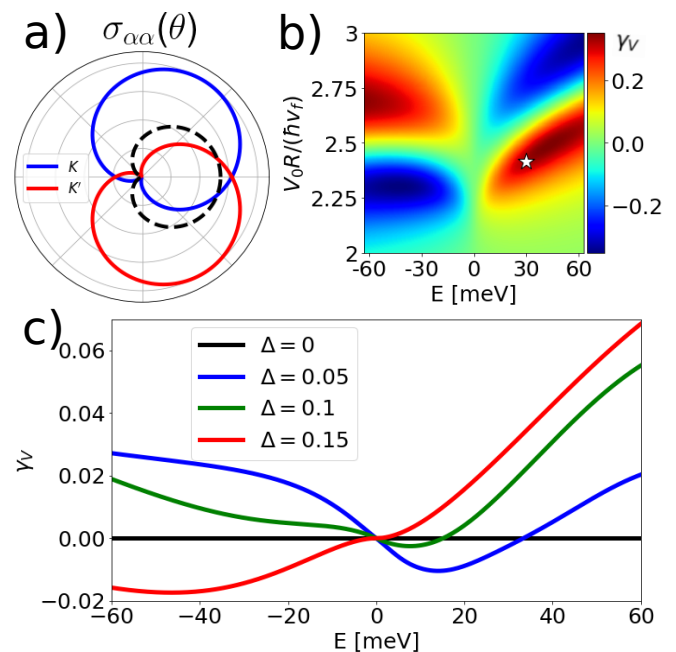

FIG. 4. a) Differential cross section for valley preserving processes, K-valley (blue) and K'-valley (red), showing the tilt of electrons with opposite valley-polarization towards opposite directions around the x-axis. The dashed black line in a) corresponds to the differential cross section without Kekulé distortion. b) Valley skew parameter γ_V as function of both energy and the gate potential for a region of $R = 9$Å and Kekulé amplitude $\Delta = 0.1$, the star marker indicates the values used for a). c) Average of γ_V as a function of energy for 4000 randomly sized Kek-Y regions ($9 \leq R \leq 18$) Å, considering $V = 1$ eV and different values of Δ.

In the presence of the Kekulé-Y modulation, the valley asymmetry of scattering around the x-axis can be also deduced from the valley dependent differential cross section. In Fig 4 a), we present the differential cross section per valley for the set of parameters indicated by a star marker in Fig. 4 b). In contrast, we notice a symmetric

scattering in the absence of the Kekulé-Y modulation, which is shown by the dashed black line in Fig 4 a). To show the dependence of the skew scattering in our system on the local potential of the Kekulé-Y patterned patches V_0, and the Fermi energy (E), in Fig. 4 b) we show a map of the skew parameter, γ_V, as a function of V_0 and E for Kekulé patterned regions with $R = 9$ Å and $\Delta = 0.1$. In the latter we should note that the regions of high γ_V coincide with the regions of resonant scattering, *i.e.*, resonant regime in the total cross section (Fig. 3), and which indicates that skew scattering is resonantly enhanced[65]. To demonstrate the robustness of skew scattering in the system to variations in size of the Kekulé-Y patterned patches, we consider a uniform random distribution of impurity sizes in the dilute limit. In Fig. 4 c) we show the average of γ_V for different values of Δ and V_0. Since skew scattering is resonantly enhanced, then its detection survives the random variations in the sizes of the Kekulé patterned patches in the dilute limit, and which allows for the detection of valley Hall effect signatures in transport experiments. We also note that since the $RV_0/(\hbar v_f)$ governs the appearance of the different scattering regimes in Fig. 3, then skew scattering is also robust to variations in the locally enhanced potential.

VI. CONCLUSIONS

We have studied the scattering of Dirac Fermions from Kekulé distorted and gated regions in graphene. For large Kekulé patterned and gated regions, we have shown that the scattering of electrons from these circular patches leads to the formation of caustics and cusps reminiscent of a circular birefringent electronic lens with two negative indices of refraction. Moreover, the separation of the cusps in the circular lens is proportional to the Kekulé interaction and provides a direct measure of its strength in systems with tailored Kekulé patches.

For low carrier concentrations, we have shown that the presence of scatterers with a locally enhanced Kekulé interaction and gate potential leads to the electrons from different valleys deflecting in opposite directions due to the skew scattering that is enhance by the Kekulé distortion. Skew scattering in the system, leads to the appearance of a valley Hall effect. We have also shown that the skew scattering-generated valley Hall effect can be detected in systems where the Kekulé patterning is not perfect, but it instead leads to the formation Kekulé patches of random sizes and potentials. The latter suggests the plausible experimental realization and detection of the skew scattering induced valley Hall effect in Kekulé patterned graphing systems via four probe experiments.

VII. ACKNOWLEDGMENTS

Appendix A: Boundary Conditions

In this appendix we find explicit solutions for the coefficients in Sec. III, which are found by solving for the boundary conditions. The solution of the system of equations resulting from the boundary condition $\Psi_n^<(R,\theta) = \Psi_n^>(R,\theta)$ gives us the following analytical expressions for the S_n matrix elements and the amplitudes $T_n^\pm$,

$$
\begin{aligned}
S_{n,K'K'} =& ss'(H_n^{(1)} H_{n-1}^{(2)} X_n + H_{n+1}^{(1)} H_n^{(2)} X_{n-1})/D_n \\
& - (2H_{n+1}^{(1)} H_{n-1}^{(2)} Q_n + H_n^{(1)} H_n^{(2)} Z_n)/D_n,
\end{aligned} \tag{A1a}
$$

$$
\begin{aligned}
S_{n,KK} =& ss'(H_{n-1}^{(1)} H_n^{(2)} X_n + H_n^{(1)} H_{n+1}^{(2)} X_{n-1})/D_n \\
& - (2H_{n-1}^{(1)} H_{n+1}^{(2)} Q_n + H_n^{(1)} H_n^{(2)} Z_n)/D_n,
\end{aligned} \tag{A1b}
$$

$$
S_{n,K'K} = \frac{-ss'Y_n P_n}{D_n}, \tag{A1c}
$$

$$
S_{n,KK'} = \frac{-ss'Y_{n-1} P_{n+1}}{D_n}, \tag{A1d}
$$

$$
\begin{aligned}
T_n^+ =& c_1(j_{n+1}^- H_n^{(1)} - ss'j_n^- H_{n+1}^{(1)})P_n/D_n \\
& + c_2(j_{n-1}^- H_n^{(1)} - ss'j_n^- H_{n-1}^{(1)})P_{n+1}/D_n,
\end{aligned} \tag{A1e}
$$

$$
\begin{aligned}
T_n^- =& c_1(j_{n+1}^+ H_n^{(1)} - ss'j_n^+ H_{n+1}^{(1)})P_n/D_n \\
& - c_2(j_{n-1}^+ H_n^{(1)} - ss'j_n^+ H_{n-1}^{(1)})P_{n+1}/D_n,
\end{aligned} \tag{A1f}
$$

where we defined,

$$
\begin{aligned}
D_n =& -ss'(H_n^{(1)} H_{n-1}^{(1)} X_n + H_{n+1}^{(1)} H_n^{(1)} X_{n-1}) \\
& + 2H_{n+1}^{(1)} H_{n-1}^{(1)} Q_n + H_n^{(1)} H_n^{(1)} Z_n,
\end{aligned} \tag{A2a}
$$

$$
X_n = j_n^+ j_{n+1}^- + j_{n+1}^+ j_n^-, \tag{A2b}
$$

$$
Y_n = j_n^+ j_{n+1}^- - j_{n+1}^+ j_n^-, \tag{A2c}
$$

$$
Z_n = j_{n-1}^+ j_{n+1}^- + j_{n+1}^+ j_{n-1}^-, \tag{A2d}
$$

$$
Q_n = j_n^+ j_n^-, \tag{A2e}
$$

$$
P_n = H_n^{(1)} H_{n-1}^{(2)} - H_{n-1}^{(1)} H_n^{(2)}, \tag{A2f}
$$

here all Hankel functions are evaluated at kR and $j_n^\pm = J_n(k_\pm R)$.

[*] eandrade@estudiantes.fisica.unam.mx

[1] Daniela Dragoman and Mircea Dragoman. *Quantum-classical analogies*. Springer Science & Business Media, 2004.

[2] MI Katsnelson, KS Novoselov, and AK Geim. Chiral tunnelling and the klein paradox in graphene. *Nature physics*, 2(9):620–625, 2006.

[3] K. S. Novoselov, A. K. Geim, S. V. Morozov, D. Jiang, Y. Zhang, S. V. Dubonos, I. V. Grigorieva, and A. A. Firsov. Electric field effect in atomically thin carbon films. *Science*, 306(5696):666–669, 2004.

[4] Vadim V Cheianov, Vladimir Fal'ko, and BL Altshuler. The focusing of electron flow and a veselago lens in graphene pn junctions. *Science*, 315(5816):1252–1255, 2007.

[5] Gil-Ho Lee, Geon-Hyoung Park, and Hu-Jong Lee. Observation of negative refraction of dirac fermions in graphene. *Nature Physics*, 11(11):925–929, 2015.

[6] Shu-Hui Zhang, Wen Yang, and F. M. Peeters. Veselago focusing of anisotropic massless dirac fermions. *Phys. Rev. B*, 97:205437, May 2018.

[7] Shu-Hui Zhang and Wen Yang. Anomalous caustics and veselago focusing in 8-pmmn borophene p–n junctions with arbitrary junction directions. *New Journal of Physics*, 21(10):103052, oct 2019.

[8] Y. Betancur-Ocampo. Partial positive refraction in asymmetric veselago lenses of uniaxially strained graphene. *Phys. Rev. B*, 98:205421, Nov 2018.

[9] F Libisch, T Hisch, R Glattauer, L A Chizhova, and J Burgdörfer. Veselago lens and klein collimator in disordered graphene. *Journal of Physics: Condensed Matter*, 29(11):114002, feb 2017.

[10] JR Williams, Tony Low, MS Lundstrom, and CM Marcus. Gate-controlled guiding of electrons in graphene. *Nature nanotechnology*, 6(4):222–225, 2011.

[11] József Cserti, András Pályi, and Csaba Péterfalvi. Caustics due to a negative refractive index in circular graphene p-n junctions. *Physical review letters*, 99(24):246801, 2007.

[12] M.V. Berry and C. Upstill. Iv catastrophe optics: Morphologies of caustics and their diffraction patterns. volume 18 of *Progress in Optics*, pages 257–346. Elsevier, 1980.

[13] Yu. A. Bychkov and E. I. Rashba. Properties of a 2d electron gas with lifted spectral degeneracy. *JETP Lett.*, 39:78–81, 1984.

[14] C. L. Kane and E. J. Mele. Quantum spin hall effect in graphene. *Phys. Rev. Lett.*, 95:226801, Nov 2005.

[15] Mahmoud M Asmar and Sergio E Ulloa. Rashba spin-orbit interaction and birefringent electron optics in graphene. *Physical Review B*, 87(7):075420, 2013.

[16] Mahmoud M Asmar and Sergio E Ulloa. Symmetry-breaking effects on spin and electronic transport in graphene. *Physical Review B*, 91(16):165407, 2015.

[17] A. H. Castro Neto, F. Guinea, N. M. R. Peres, K. S. Novoselov, and A. K. Geim. The electronic properties of graphene. *Rev. Mod. Phys.*, 81:109–162, Jan 2009.

[18] Mikhail I Katsnelson and Mikhail Iosifovich Katsnelson. *Graphene: carbon in two dimensions*. Cambridge university press, 2012.

[19] Vinod Kumar Joshi. Spintronics: A contemporary review of emerging electronics devices. *Engineering Science and Technology, an International Journal*, 19(3):1503 – 1513, 2016.

[20] Igor Žutić, Jaroslav Fabian, and S. Das Sarma. Spintronics: Fundamentals and applications. *Rev. Mod. Phys.*, 76:323–410, Apr 2004.

[21] A. Rycerz, J. Tworzydło, and C. W. J. Beenakker. Valley filter and valley valve in graphene. *Nature Phys.*, 3, 2007.

[22] D. Gunlycke and C. T. White. Graphene valley filter using a line defect. *Phys. Rev. Lett.*, 106:136806, Mar 2011.

[23] J.-H. Chen, G. Autès, N. Alem, F. Gargiulo, A. Gautam, M. Linck, C. Kisielowski, O. V. Yazyev, S. G. Louie, and A. Zettl. Controlled growth of a line defect in graphene and implications for gate-tunable valley filtering. *Phys. Rev. B*, 89:121407, Mar 2014.

[24] Yang Liu, Juntao Song, Yuxian Li, Ying Liu, and Qing-Feng Sun. Controllable valley polarization using graphene multiple topological line defects. *Phys. Rev. B*, 87:195445, May 2013.

[25] Zhe Liu, Liwei Jiang, and Yisong Zheng. Tunable valley polarization by a gate voltage when an electron tunnels through multiple line defects in graphene. *J. Phys.: Cond. Matt.*, 27(4):045501, 2015.

[26] Feng Zhai, Xiaofang Zhao, Kai Chang, and H. Q. Xu. Magnetic barrier on strained graphene: A possible valley filter. *Phys. Rev. B*, 82:115442, Sep 2010.

[27] M. Ramezani Masir, A. Matulis, and F. M. Peeters. Scattering of Dirac electrons by circular mass barriers: Valley filter and resonant scattering. *Phys. Rev. B*, 84:245413, Dec 2011.

[28] D. Moldovan, M. Ramezani Masir, L. Covaci, and F. M. Peeters. Resonant valley filtering of massive Dirac electrons. *Phys. Rev. B*, 86:115431, Sep 2012.

[29] J. Wang and S. Fischer. Topological valley resonance effect in graphene. *Phys. Rev. B*, 89:245421, Jun 2014.

[30] J. L. Garcia-Pomar, A. Cortijo, and M. Nieto-Vesperinas. Fully valley-polarized electron beams in graphene. *Phys. Rev. Lett.*, 100:236801, Jun 2008.

[31] Yongjin Jiang, Tony Low, Kai Chang, Mikhail I. Katsnelson, and Francisco Guinea. Generation of pure bulk valley current in graphene. *Phys. Rev. Lett.*, 110:046601, Jan 2013.

[32] Marko M. Grujić, MilanŽ. Tadić, and François M. Peeters. Spin-valley filtering in strained graphene structures with artificially induced carrier mass and spin-orbit coupling. *Phys. Rev. Lett.*, 113:046601, Jul 2014.

[33] Mahmoud M. Asmar and Sergio E. Ulloa. Minimal geometry for valley filtering in graphene. *Phys. Rev. B*, 96:201407, Nov 2017.

[34] Chang-Yu Hou, Claudio Chamon, and Christopher Mudry. Electron fractionalization in two-dimensional graphenelike structures. *Phys. Rev. Lett.*, 98:186809, May 2007.

[35] Claudio Chamon. Solitons in carbon nanotubes. *Phys. Rev. B*, 62:2806–2812, Jul 2000.

[36] O V Gamayun, V P Ostroukh, N V Gnezdilov, İ Adagideli, and C W J Beenakker. Valley-momentum locking in a graphene superlattice with y-shaped kekulé bond texture. *New Journal of Physics*, 20(2):023016, 2018.

[37] Christopher Gutiérrez, Cheol-Joo Kim, Lola Brown, Theanne Schiros, Dennis Nordlund, Edward B Lochocki, Kyle M Shen, Jiwoong Park, and Abhay N Pasupathy. Imaging chiral symmetry breaking from kekulé bond order

in graphene. *Nature Physics*, 12(10):950, 2016.

[38] Changhua Bao, Hongyun Zhang, Teng Zhang, Xi Wu, Laipeng Luo, Shaohua Zhou, Qian Li, Yanhui Hou, Wei Yao, Liwei Liu, Pu Yu, Jia Li, Wenhui Duan, Hong Yao, Yeliang Wang, and Shuyun Zhou. Experimental evidence of chiral symmetry breaking in kekulé-ordered graphene. *Phys. Rev. Lett.*, 126:206804, May 2021.

[39] Changhua Bao, Hongyun Zhang, Xi Wu, Shaohua Zhou, Qian Li, Pu Yu, Jia Li, Wenhui Duan, and Shuyun Zhou. Coexistence of extended flat band and kekulé order in li-intercalated graphene. *Phys. Rev. B*, 105:L161106, Apr 2022.

[40] Daejin Eom and Ja-Yong Koo. Direct measurement of strain-driven kekulé distortion in graphene and its electronic properties. *Nanoscale*, 12:19604–19608, 2020.

[41] AC Qu, P Nigge, S Link, G Levy, M Michiardi, PL Spandar, T Matthé, M Schneider, S Zhdanovich, U Starke, et al. Ubiquitous defect-induced density wave instability in monolayer graphene. *Science Advances*, 8(23):eabm5180, 2022.

[42] Mo-Han Zhang, Ya-Ning Ren, Qi Zheng, Xiao-Feng Zhou, and Lin He. Stabilizing sample-wide Kekulé orders in graphene/transition metal dichalcogenide heterostructures, August 2022. arXiv:2208.01286.

[43] Yawar Mohammadi and Samira Bahrami. Integer quantum hall effect in kekulé-patterned graphene. *Chinese Physics B*, 31(1):017305, 2022.

[44] Elias Andrade, Ramon Carrillo-Bastos, Pierre A. Pantaleón, and Francisco Mireles. Resonant transport in kekulé-distorted graphene nanoribbons. *Journal of Applied Physics*, 127(5):054304, 2020.

[45] Saúl A. Herrera and Gerardo G. Naumis. Electronic and optical conductivity of kekulé-patterned graphene: Intravalley and intervalley transport. *Phys. Rev. B*, 101:205413, May 2020.

[46] Saúl A. Herrera and Gerardo G. Naumis. Dynamic polarization and plasmons in kekulé-patterned graphene: Signatures of broken valley degeneracy. *Phys. Rev. B*, 102:205429, Nov 2020.

[47] Yawar Mohammadi. Magneto-optical conductivity of graphene: Signatures of a uniform y-shaped kekule lattice distortion. *ECS Journal of Solid State Science and Technology*, 10(6):061011, jun 2021.

[48] Alex Santacruz, Priscilla E. Iglesias, Ramon Carrillo-Bastos, and Francisco Mireles. Valley-driven zitterbewegung in kekulé-distorted graphene. *Phys. Rev. B*, 105:205405, May 2022.

[49] Juan Juan Wang, S. Liu, J. Wang, and Jun-Feng Liu. Valley-coupled transport in graphene with y-shaped kekulé structure. *Phys. Rev. B*, 98:195436, Nov 2018.

[50] Elias Andrade, Ramon Carrillo-Bastos, and Gerardo G. Naumis. Valley engineering by strain in kekulé-distorted graphene. *Phys. Rev. B*, 99:035411, Jan 2019.

[51] David A. Ruiz-Tijerina, Elias Andrade, Ramon Carrillo-Bastos, Francisco Mireles, and Gerardo G. Naumis. Multi-flavor dirac fermions in kekulé-distorted graphene bilayers. *Phys. Rev. B*, 100:075431, Aug 2019.

[52] Qing-Ping Wu, Lu-Lu Chang, Yu-Zeng Li, Zheng-Fang Liu, and Xian-Bo Xiao. Electric-controlled valley pseudomagnetoresistance in graphene with Y-shaped kekulé lattice distortion. *Nanoscale research letters*, 15(1):1–6, 2020.

[53] Juan Juan Wang, S. Liu, J. Wang, and Jun-Feng Liu. Valley supercurrent in the kekulé graphene superlattice heterojunction. *Phys. Rev. B*, 101:245428, Jun 2020.

[54] W. Zeng and R. Shen. Enhanced andreev reflection in kekulé-y patterned graphene. *Phys. Rev. B*, 104:075436, Aug 2021.

[55] Santiago Galván y García, Thomas Stegmann, and Yonatan Betancur-Ocampo. Generalized hamiltonian for kekulé graphene and the emergence of valley-cooperative klein tunneling. *Phys. Rev. B*, 105:125139, Mar 2022.

[56] Elías Andrade, Gerardo G Naumis, and Ramon Carrillo-Bastos. Electronic spectrum of kekulé patterned graphene considering second neighbor-interactions. *Journal of Physics: Condensed Matter*, 33(22):225301, 2021.

[57] H. Ochoa, A. H. Castro Neto, V. I. Fal'ko, and F. Guinea. Spin-orbit coupling assisted by flexural phonons in graphene. *Phys. Rev. B*, 86:245411, Dec 2012.

[58] CWJ Beenakker. Colloquium: Andreev reflection and klein tunneling in graphene. *Reviews of Modern Physics*, 80(4):1337, 2008.

[59] Edward McCann and Vladimir I Fal'ko. Symmetry of boundary conditions of the dirac equation for electrons in carbon nanotubes. *Journal of Physics: Condensed Matter*, 16(13):2371, 2004.

[60] David J. Alspaugh, Mahmoud M. Asmar, Daniel E. Sheehy, and Ilya Vekhter. Andreev spectroscopy of non-helical spin textures in topological insulators. *Phys. Rev. B*, 105:054502, Feb 2022.

[61] Eklavya Thareja, Ilya Vekhter, and Mahmoud M. Asmar. Conductance of gated junctions as a probe of topological interface states. *Phys. Rev. B*, 102:125308, Sep 2020.

[62] Mostafa Tanhayi Ahari, Gerardo Ortiz, and Babak Seradjeh. On the role of self-adjointness in the continuum formulation of topological quantum phases. *American Journal of Physics*, 84(11):858–868, 2016.

[63] L. Isaev, G. Ortiz, and I. Vekhter. Tunable unconventional kondo effect on topological insulator surfaces. *Phys. Rev. B*, 92:205423, Nov 2015.

[64] Mahmoud M. Asmar and Sergio E. Ulloa. Spin-orbit interaction and isotropic electronic transport in graphene. *Phys. Rev. Lett.*, 112:136602, Apr 2014.

[65] Aires Ferreira, Tatiana G Rappoport, Miguel A Cazalilla, and AH Castro Neto. Extrinsic spin hall effect induced by resonant skew scattering in graphene. *Physical review letters*, 112(6):066601, 2014.